

# IMAGING AND SPECTROSCOPIC DIAGNOSTICS ON THE FORMATION OF TWO MAGNETIC FLUX ROPES REVEALED BY *SDO*/AIA AND *IRIS*

X. CHENG<sup>1,2,3</sup>, M. D. DING<sup>1,3</sup>, & C. FANG<sup>1,3</sup>

<sup>1</sup>School of Astronomy and Space Science, Nanjing University, Nanjing 210093, China

<sup>2</sup>Key Laboratory of Solar Activity, National Astronomical Observatories, Chinese Academy of Sciences, Beijing 100012, China and

<sup>3</sup>Key Laboratory for Modern Astronomy and Astrophysics (Nanjing University), Ministry of Education, Nanjing 210093, China

*Submitted to ApJ*

## ABSTRACT

Helical magnetic flux rope (MFR) is a fundamental structure of corona mass ejections (CMEs) and has been discovered recently to exist as a sigmoidal channel structure prior to its eruption in the extreme ultraviolet (EUV) high temperature passbands of the Atmospheric Imaging Assembly (AIA). However, when and where the MFR is built up are still elusive. In this paper, we investigate two MFRs (MFR1 and MFR2) in detail, whose eruptions produced two energetic solar flares and CMEs on 2014 April 18 and 2014 September 10, respectively. The AIA EUV images reveal that for a long time prior to their eruption, both MFR1 and MFR2 are under formation, which is probably through magnetic reconnection between two groups of sheared arcades driven by the shearing and converging flows in the photosphere near the polarity inversion line. At the footpoints of the MFR1, the *Interface Region Imaging Spectrograph* Si IV, C II, and Mg II lines exhibit weak to moderate redshifts and a non-thermal broadening in the pre-flare phase. However, a relatively large blueshift and an extremely strong non-thermal broadening are found at the formation site of the MFR2. These spectral features consolidate the proposition that the reconnection plays an important role in the formation of MFRs. For the MFR1, the reconnection outflow may propagate along its legs, penetrating into the transition region and the chromosphere at the footpoints. For the MFR2, the reconnection probably takes place in the lower atmosphere and results in the strong blueshift and non-thermal broadening for the Mg II, C II, and Si IV lines.

*Subject headings:* Sun: corona — Sun: coronal mass ejections (CMEs) — Sun: magnetic fields — Sun: UV radiation

## 1. INTRODUCTION

Magnetic flux rope (MFR) is a current channel with magnetic field lines wrapping around its central axis by more than one turn. Such a coherently helical structure frequently erupts from the Sun, forming a coronal mass ejection (CME) in the lower corona (Cheng et al. 2013a; Liu et al. 2014a; Chen 2011), and then propagating into the interplanetary space taking a form of magnetic cloud as indicated by features including the magnetic field rotation, the drop of density and proton temperature, and the low plasma beta in the in-situ data (Burlaga et al. 1981; Zhang et al. 2007; Liu et al. 2014b).

Previous observations have shown that MFRs probably exist in the corona prior to their eruption. Based on the different origins, MFRs can be divided into two categories. One type originates from long decayed active regions and appears as dark cavities in visible or extreme ultraviolet (EUV) passbands when viewed at the solar limb (Gibson et al. 2006; Régnier et al. 2011; Mackay et al. 2010). The spinning motions (Wang & Stenborg 2010; Li et al. 2012), bright ring (Dove et al. 2011), and “lagomorphic” structure of linear polarization in the cavities (Bak-Stęślicka et al. 2013) have been disclosed and considered to be strong evidence of helical structures. This type of MFRs also displays as filament channels when seen at the solar disk, the counterpart of the cavities, in which the emission is much weaker than the background in EUV passbands

but the magnetic field is well organized and probably includes dips (Low & Hundhausen 1995; Gibson & Fan 2006). Distinguishing from cavities, the other group of MFRs stems from mature active regions, manifesting themselves as forward or reversed sigmoids in soft X-ray (SXR) and EUV passbands (Canfield et al. 1999; Sterling et al. 2000; Fan & Gibson 2004; Kliem et al. 2004). A number of independent case studies have shown that the strongly twisted field lines and the sigmoidal emission pattern can be successfully reproduced in extrapolated non-linear force free structures (Guo et al. 2010; Savcheva et al. 2012; Su & van Ballegooijen 2012; Cheng et al. 2013b; Jiang et al. 2014; Inoue et al. 2013; Amari et al. 2014).

Recently, Zhang et al. (2012) and Cheng et al. (2013a) discovered another piece of observational evidence for the existence of MFRs in mature active regions, i.e., an elongated EUV channel-like structure in the high temperature passbands of the Atmospheric Imaging Assembly (AIA; Lemen et al. 2012). The hot channel initially appears as a twisted sigmoidal structure and then evolves to a semicircular one in the early rise phase. Quickly, it drives the formation and acceleration of a CME with the aid of the flare reconnection (Cheng et al. 2011, 2013a; Li & Zhang 2013a). Further studies including the continuous evolution of the MFR from the inner to outer corona as a coherent structure (Cheng et al. 2014c), the relationship between the hot channel and associated prominence (Cheng et al. 2014a; Kumar et al. 2011; Li & Zhang 2013b; Yang et al. 2014), and the find-

ing of reduced temperature but enhanced emission measure at the lower part of filament-associated hot channel (Chen et al. 2014a) further support that the hot channel is actually the helical MFR itself.

Although much evidence has revealed the existence of MFRs, when and where they are built up are still unknown. Theoretically, one possibility could be that the MFR is generated in the convection zone and partly emerges into the corona by buoyancy (e.g., Fan 2001; Manchester et al. 2004; Archontis & Török 2008; Leake et al. 2013). The other possibility is that the MFR is created directly in the corona either through flux cancellation in the photosphere prior to the eruption (Wang & Shi 1993; Green & Kliem 2009; Green et al. 2011; Aulanier et al. 2010; Amari et al. 2011; Xia et al. 2014; Amari et al. 2014) or by tether-cutting (Moore et al. 2001; Liu et al. 2010), breakout (Antiochos et al. 1999; Lynch et al. 2008; Karpen et al. 2012), and flare reconnection (Patsourakos et al. 2013; Kumar & Cho 2014; Song et al. 2014) in the corona during the eruption. In this paper, we investigate the formation and initiation of two MFRs and in particular, present for the first time the spectral features related to this process. The results suggest that the reconnection in the lower atmosphere may play an important role in forming and initiating the MFRs. The instruments and data reduction are introduced in Section 2. AIA Observations of the MFRs are shown in Section 3, followed by *IRIS* observations of the MFRs in Section 4. Summary and discussions are given in Section 5.

## 2. INSTRUMENTS AND DATA REDUCTION

The data sets are primarily from *Solar Dynamics Observatory* (*SDO*; Pesnell et al. 2012) and newly launched Interface Region Imaging Spectrograph (*IRIS*; De Pontieu et al. 2014). The AIA on board *SDO* images the solar atmosphere at temperatures ranging from 0.06 MK to 20 MK through 10 passbands (7 EUV passbands and 3 UV passbands). Each EUV (UV) image has a temporal cadence of 12 s (24 s) and spatial resolution of 1.2". The Helioseismic and Magnetic Imager (HMI; Schou et al. 2012) also on board *SDO* measures the vector magnetic field of the full solar disk. Here, we only take advantage of the line-of-sight magnetograms with the cadence of 720 s. Moreover, the *GOES* provides the soft X-ray (SXR) 1–8 Å flux of the whole Sun during the solar eruptions.

*IRIS* obtains spectra and images from the photosphere, chromosphere, transition region, to corona with an unprecedented high spatial resolution of 0.33–0.4", temporal cadence of  $\sim 2$  s, and spectral resolution of  $\sim 1$  km s $^{-1}$  over a field of view of 175"  $\times$  175" (De Pontieu et al. 2014). The sit-and-stare mode is set during the periods of the formation and initiation of the two MFRs. The spectra include three doublet bright lines, Mg II h/k ( $\sim 10^4$  K) line forming in the chromosphere and C II 1334/1335 ( $\sim 10^{4.3}$  K) and Si IV 1394/1403 Å ( $\sim 10^{4.8}$  K) lines in the transition region. In this study, we only analyze one component of the doublet lines, i.e., Mg II k 2796.347 Å, C II 1335.7077 Å, and Si IV 1402.77 Å. The slit-jaw images (SJIs) with a cadence of 12 s in the 2796 Å, 1400 Å, and 1330 Å passbands are taken simultaneously. All the spectra and images that we take for study are from calibrated level 2 data, which have already taken

into account dark current subtraction, flat-field correction, and geometrical correction (De Pontieu et al. 2014; Tian et al. 2014b). The wavelength calibration is critical for properly measuring the Doppler velocities. Here, the wavelengths of the C II and Si IV lines are calibrated by assuming a zero velocity of the nearby O I 1355.5977 Å and Fe II 1405.608 Å lines, respectively. For the Mg II line that is more perturbed by plasma dynamics, we calculate the average profile along the whole slit and find it can well represent the reference profile with an uncertainty of only 1–2 km s $^{-1}$ . Moreover, we also eliminate the orbital variation of the line positions caused by the temperature change of the detector and the change of the distance between the spacecraft and the Sun with the routine *iris\_orbital\_corr\_l2.pro* (Tian et al. 2015) in the SSW package.

## 3. AIA OBSERVATIONS OF THE MFRS

In this section, we concentrate on EUV imaging of the formation of two MFRs (MFR1 and MFR2), whose eruptions produced a CME and an M7.3 flare on 2014 April 18 and a CME and an X1.6 flare on 2014 September 10, respectively. The *GOES* soft X-ray fluxes of the two flares are shown in Figure 1.

### 3.1. 2014 April 18 MFR

For the 2014 April 18 event, two groups of sheared arcades can be seen in the core field of associated active region at  $\sim 07:30$  UT. After  $\sim 30$  minutes, a confined flare (C4.8 class) begins and results in a quick brightening of the sheared arcades. In addition, some forward sigmoidal threads located above the arcades appear. It implies that part of the twisted field lines of MFR1 have probably been formed in the course of the confined flare (also see; Patsourakos et al. 2013). After the flare, both the sheared arcades and sigmoidal threads disappear. At  $\sim 11:20$  UT, the sheared arcades appear again. After  $\sim 15$  minutes, some forward sigmoidal threads also show up. With the threads being further brightened, the concave middle part gradually becomes flat and detaches from the underlying arcades (for details please see online movie of Figure 2). The whole evolution process is only visible in the AIA high temperature passbands (i.e., 131 Å and 94 Å) but not in other cooler passbands, indicating that the sheared arcades and sigmoidal threads are a very hot structure with a temperature of over 7 MK (Zhang et al. 2012; Cheng et al. 2013a). It suggests that the reconnection may exist continuously and help further build up the MFR1 after the confined flare.

The more interesting thing is that the right footpoints of the MFR1 start to become bright after  $\sim 11:40$  UT, which are visible in all AIA EUV and UV passbands. At the same time, some small loops underneath the central part of the MFR1 also brighten and appear as a cusp shape from the hot to cool temperature passbands in time sequence (see online movie of Figure 2). The simultaneous brightening of the cusp-shaped small loops, the sigmoidal threads, and the footpoints of MFR1 seems to support that the reconnection could be of tether-cutting type, which takes place at the center of the sigmoid to convert the surrounding sheared arcades to the twisted lines of the MFR (also see; Liu et al. 2010; Chen et al. 2014b). At 12:20 UT, a well-shaped sigmoidal MFR1 has been formed (Figure 2). After experiencing a slow rise

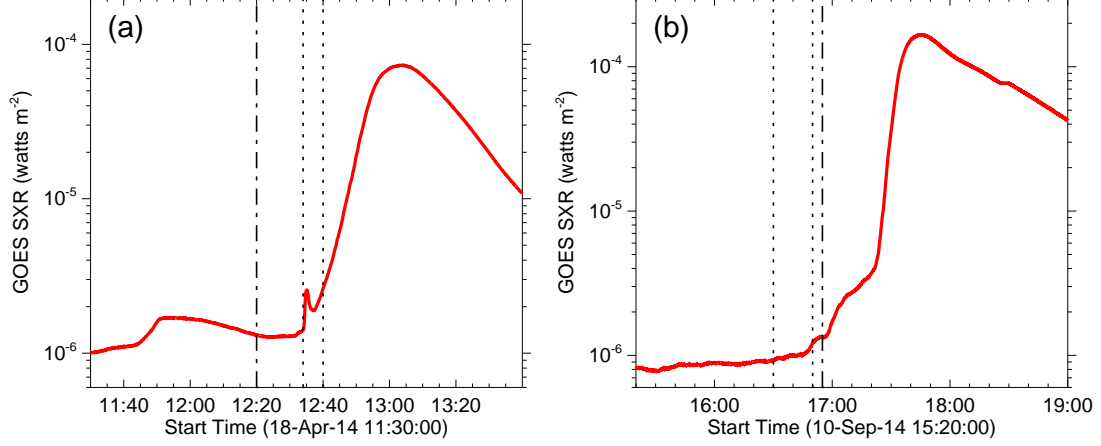


FIG. 1.— (a) *GOES* soft X-ray 1–8 Å flux of the solar flare (M7.3) on 2014 April 18. The vertical dash-dotted line denotes the instant at which the MFR1 is well formed as shown in Figure 2; the two vertical dotted lines show the time interval, during which *IRIS* observations are analyzed. (b) Same as in (a) but for the solar flare (X1.6) on 2014 September 10.

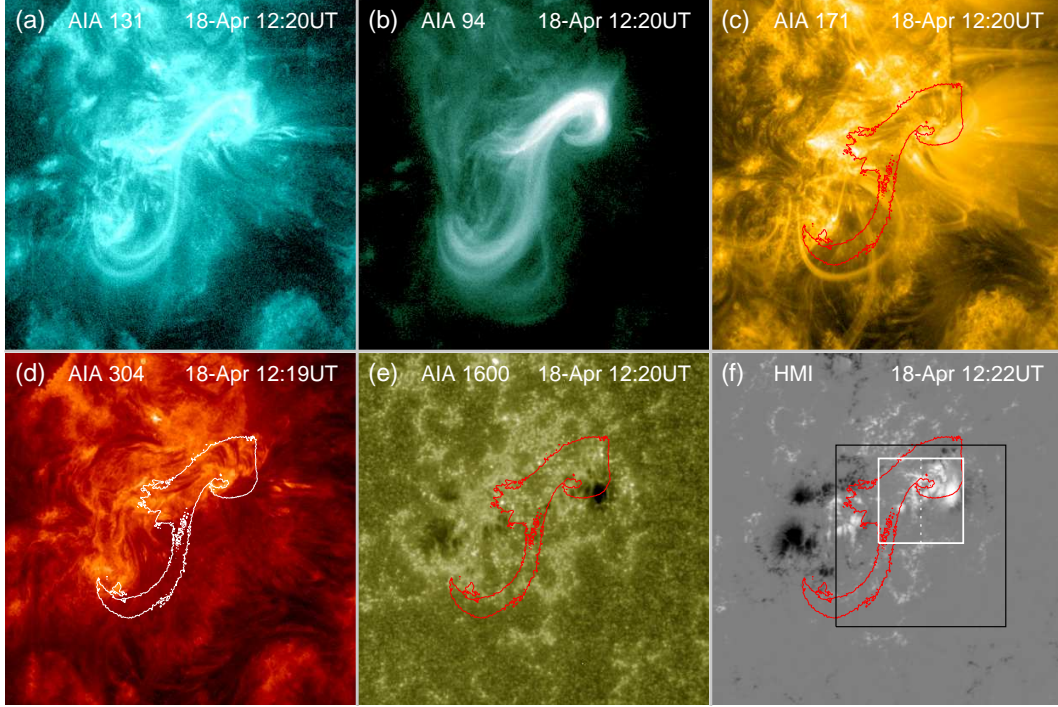


FIG. 2.— *SDO*/AIA 131 Å ( $\sim 0.4$ , 10, and 16 MK), 94 Å ( $\sim 6$  MK), 171 Å ( $\sim 0.6$  MK), 1600 Å ( $\sim 0.1$  MK), 1700 Å ( $\sim 0.5$  MK) images, and *SDO*/HMI line-of-sight magnetogram showing the MFR1 prior to the eruption (a and b), the overlying field (c), the lower atmosphere (d and e), and the magnetic field (f) in the active region NOAA 12036. The white and red contours in panels (c)–(f) indicate the location of the MFR1. The black box in panel (f) denotes the field-of-view of *IRIS* ( $128'' \times 128''$ ) and the smaller one (white;  $60'' \times 60''$ ) refers to the region which we are interesting in. The vertical dotted line indicates the position of *IRIS* slit.

(Animation of this figure is available in the online journal.)

and expansion phase, the MFR1 suddenly erupts and afterwards produces a strong flare and a CME. Note that, at  $\sim 12:32$  UT, a jet is triggered near the formation site of MFR1 and may play a role in initiating the impulsive acceleration of MFR1.

### 3.2. 2014 September 10 MFR

For the 2014 September 10 event, during the long-term evolution before the eruption, the initial structure of the core field mainly consists of two groups of sheared arcades and central sigmoidal threads. Overall, these structures make up a reversed sigmoid. The sigmoid only appears in

the AIA 94 Å passband, showing that its temperature is very close to  $\sim 7$  MK, a peak temperature of the response function of this passband. Its being invisible in the AIA 131 Å passband implies an absence of plasma with higher temperatures (e.g., 10 MK). At  $\sim 13:57$  UT, a C1.5 confined flare occurs near the right elbows of the sigmoid and make the nearby arcades brighten significantly, even in the AIA 131 Å passband. After  $\sim 15:00$  UT, the most important evolution is repetitive appearance and disappearance of the central sigmoidal threads that could be a nascent structure of the MFR2 and have been developed via the reconnection in the course of the confined flare



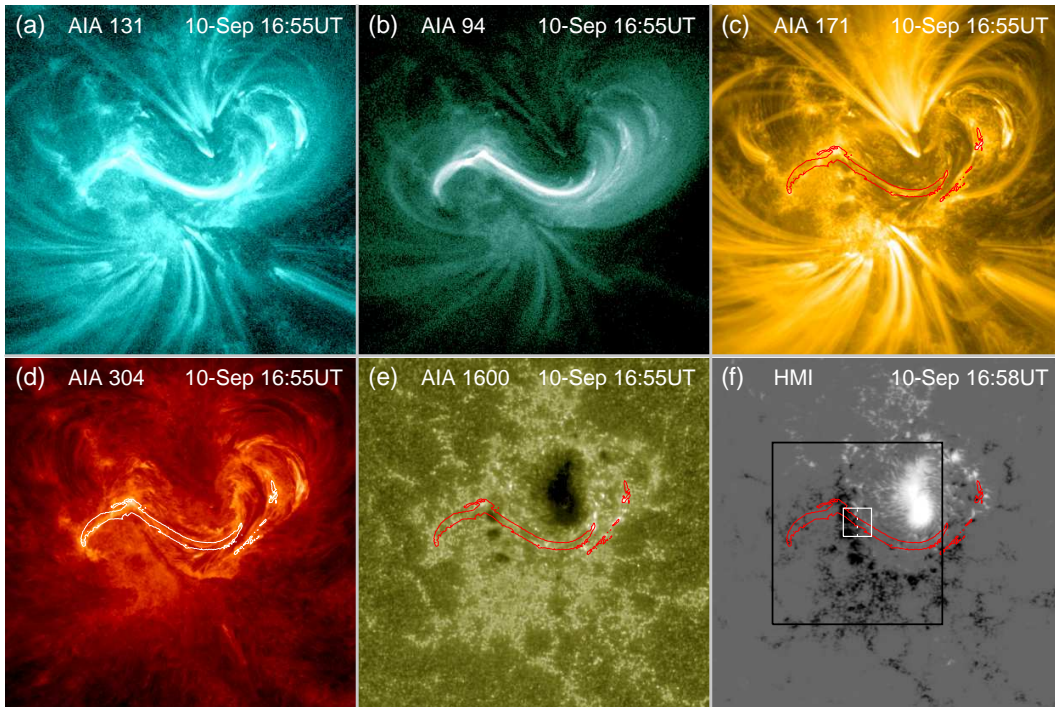


FIG. 3.— Same as Figure 2 but for the MFR2 in the active region NOAA 12158. The field of view of the black (white) box is  $128'' \times 128''$  ( $20'' \times 20''$ ).

(Animation of this figure is available in the online journal.)

(for details please see online movie of Figure 3). The sigmoidal threads initially appear at  $\sim 15:10$  UT. Subsequently, they become brighter and last for  $\sim 20$  minutes, and then disappear quickly. At  $\sim 16:05$  UT, the sigmoidal threads turn up again and last for only 10 minutes. At  $\sim 16:30$  UT, the most apparent feature is the brightening at the sigmoid center, probably the formation site of MFR2. After that ( $\sim 16:45$  UT), the sigmoidal threads get rapidly brightened and are also visible in the AIA 131 Å passband. It implies that the sigmoidal threads have been heated to  $\sim 10$  MK at that time, most likely due to the reconnection. At  $\sim 16:55$  UT, a well-shaped sigmoidal structure, MFR2, has been formed as shown in Figure 3. After experiencing a slow rise phase, it erupts and produces a strong flare and a CME. Similar to the MFR1, the intermittent appearance of the sigmoidal threads suggest the intermittent occurrence of reconnection, which not only heats the sigmoidal threads but also connects the sheared arcades to form the MFR2 prior to the eruption.

#### 4. IRIS OBSERVATIONS OF THE MFRS

##### 4.1. Transition Region and Chromospheric Imaging of the MFRs

The pre-flare phase of the MFR1 and the formation phase of the MFR2 are also well observed by *IRIS* with the sit-and-stare mode. For the MFR1, the slit is positioned crossing the right footpoints as shown in Figure 2f. The whole observations are made from 12:33 UT to 17:18 UT. For the MFR2, the slit is positioned at the possible formation site as displayed in Figure 3f. The observations last from 11:28 UT to 17:57 UT. Here, we mainly analyze the data in the intervals of 12:33–12:50 UT and 15:30–17:00 UT for the MFR1 and MFR2, respectively. From the *IRIS* 1400 Å, 1330 Å, 2796 Å images and the

AIA 304 Å and 1600 Å images, we cannot see any signatures of the MFR1 (see the online movies of Figure 2 and Figure 4). It indicates that the magnetic structure of the MFR1 mainly lies in the corona with no stretching in the transition region and chromosphere except for the footpoints. The footpoints of the MFR1 start to brighten in the transition region and chromosphere at 12:35 UT. The snapshots of the footpoints that are strongly brightened at 12:40 UT are displayed in Figures 4b, 6b, and 7b, as compared with the snapshots of the footpoints that are not yet strongly brightened in Figures 4a, 6a, and 7a.

The appearance of the MFR2 is different from that of the MFR1. Besides in the 131 Å and 94 Å passbands, some bright sigmoidal loops are also present in the 1400 Å and 2796 Å passbands (Figures 3, 8, 11, and attached movies). In the 171 Å and 304 Å passbands, some filamentary materials are also found to be cospatial with the threads in the middle part of the MFR2 (Figure 3c and 3d). Such a different emission feature implies that the height of the MFR2 may be lower than that of the MFR1, i.e., the MFR2 structure may partially extend into the transition region and even the chromosphere. It also suggests that cool materials suspend in the dips of the MFR2 while it is not the case for the MFR1. The 1400 Å and 2796 Å SJI images of the brightened MFR2 at 16:30 UT are displayed in Figures 8a, 10a, and 11a, while those after the brightening disappears ( $\sim 16:50$  UT) are shown in Figures 8b, 10b, and 11b.

##### 4.2. Spectral Properties of the MFRs

###### 4.2.1. Redshift at the Footpoints of the MFR1

The spectra of *IRIS* provide an important tool to diagnose the properties of the MFR in the lower atmosphere. Figures 4c, 6c, and 7c and Figures 4d, 6d, and 7d show the spectra of the Si IV 1402.77 Å, C II 1335.7077 Å, and

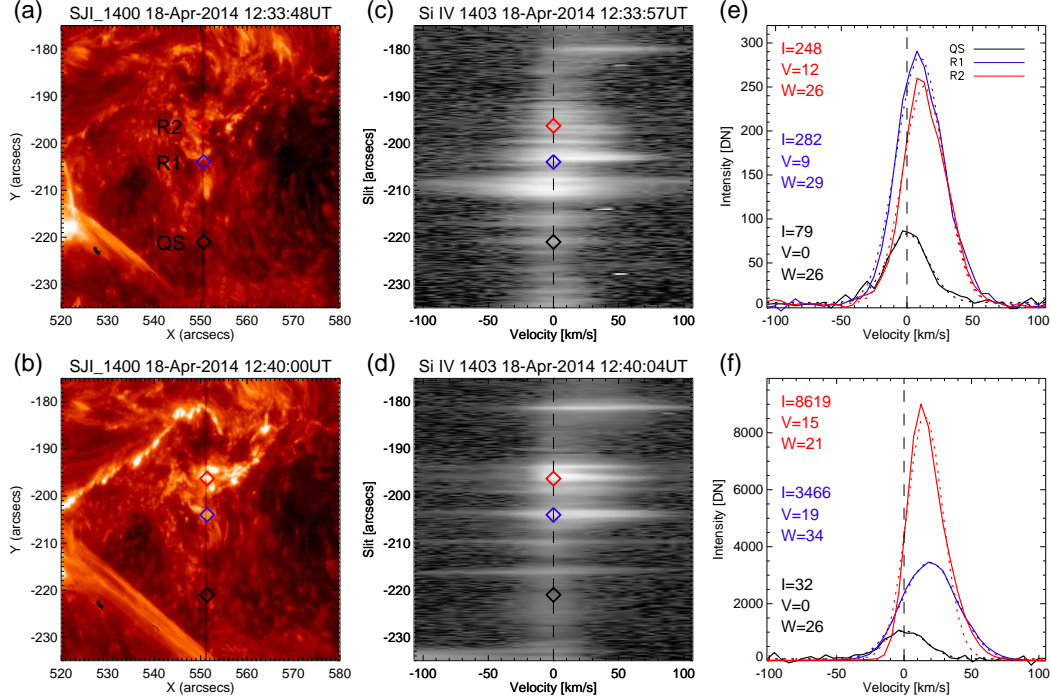


FIG. 4.— (a) and (b) *IRIS* 1400 Å SJI images displaying the footpoints of the MFR1 in the transition region. The blue (R1) and red (R2) diamonds denote the two pixels at the footpoints, and the black one (QS) indicates one pixel at the quiet region. (c) and (d) Spectra of the Si IV 1402.77 Å line at the slit as shown in panels (a) and (b). (e) and (f) Profiles of the Si IV line at R1, R2, and QS. Their single Gaussian fittings are shown by the dotted curves. Quantities  $I$ ,  $V$ , and  $W$  correspond to the peak intensity, Doppler velocity, and FWHM. Note that, in panel f, the profile of the Si IV line at QS is multiplied by 30. Moreover, in panel c, the brightened area ( $y = [-213'', -207'']$ ) in which the Si IV line is significantly blueshifted and broadened denotes the footpoints of a set of brightened coronal loops near the MFR1.

(Animation of this figure is available in the online journal.)

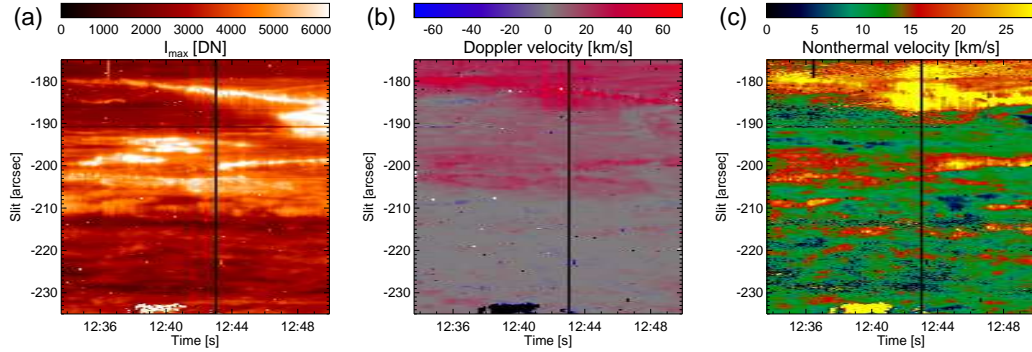


FIG. 5.— Slit-time plots of the peak intensity (a), Doppler velocity (b), and non-thermal velocity (c) of the Si IV 1402.77 Å line for the 2014 April 18 event.

Mg II k 2796.347 Å lines at the slit before and after the footpoints are strongly brightened, respectively. Along the slit, we select three pixels: one corresponds to the quiet Sun region (QS in Figure 4a), and the other two are at the footpoints of the MFR1 (R1 and R2 in Figure 4a). The profiles of the Si IV line and the fitted ones at R1, R2, and QS are plotted in Figure 4e and 4f. One can see the following spectral features: (1) the profiles are nearly Gaussian; (2) the centroids of the line tend to be redshifted at R1 and R2; and (3) the peak intensities are significantly enhanced at R1 and R2 as compared with that at QS. In order to quantitatively measure the peak intensity, the Doppler shift, and the full width at half maximum (FWHM) of the Si IV line at the three pixels, we apply a single Gaussian fitting to the profiles. The results show that before the footpoints get brightened, the

redshift velocities at R1 and R2 are 9 and 12 km s<sup>-1</sup>, and the FWHMs are 29 and 26 km s<sup>-1</sup>, respectively. With the footpoints being strongly brightened, the peak intensities increase as large as 10 times. The redshift velocities increase somewhat (19 and 15 km s<sup>-1</sup>), but the FWHMs show little change (34 and 21 km s<sup>-1</sup>).

In order to study the temporal and spatial variation of the Si IV line, we apply a single Gaussian fitting to the profiles at the slit of interest ( $y = [-235'', -175'']$ ) and obtain the slit-time plots of the peak intensity, the Doppler velocity, and the non-thermal velocity (Figure 5). A bright ribbon exhibiting a very strong peak intensity and a relatively large Doppler velocity and non-thermal velocity can be identified. It actually denotes the flare ribbon sweeping across the slit. Besides the flare ribbon, one can see that the footpoints of the MFR1 also present

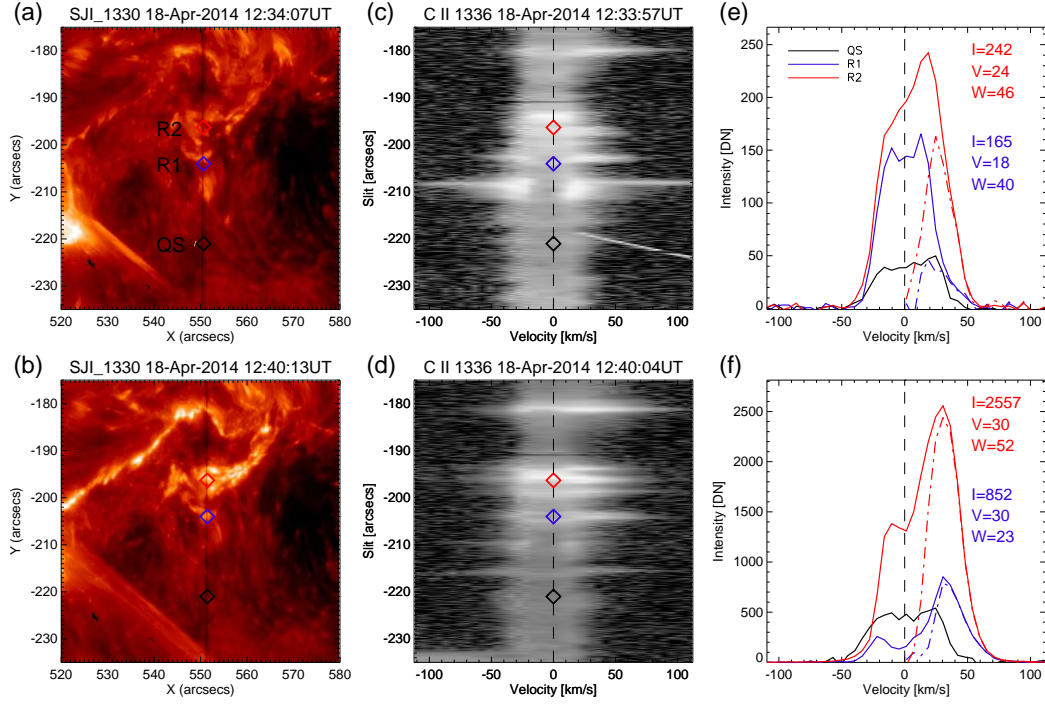


FIG. 6.— (a) and (b) *IRIS* 1330 Å SJI images displaying the footpoints of the MFR1 in the lower transition region. The red, blue, and black diamonds have the same meanings as in Figure 4. (c) and (d) Spectra of C II 1335.7077 Å at the slit. (e) and (f) Profiles of C II 1335.7077 Å at R1, R2, and QS. The dash-dotted curves denote the difference between the red wing and the blue wing. Note that, in panel f, the profile of the C II line at QS is multiplied by 10.

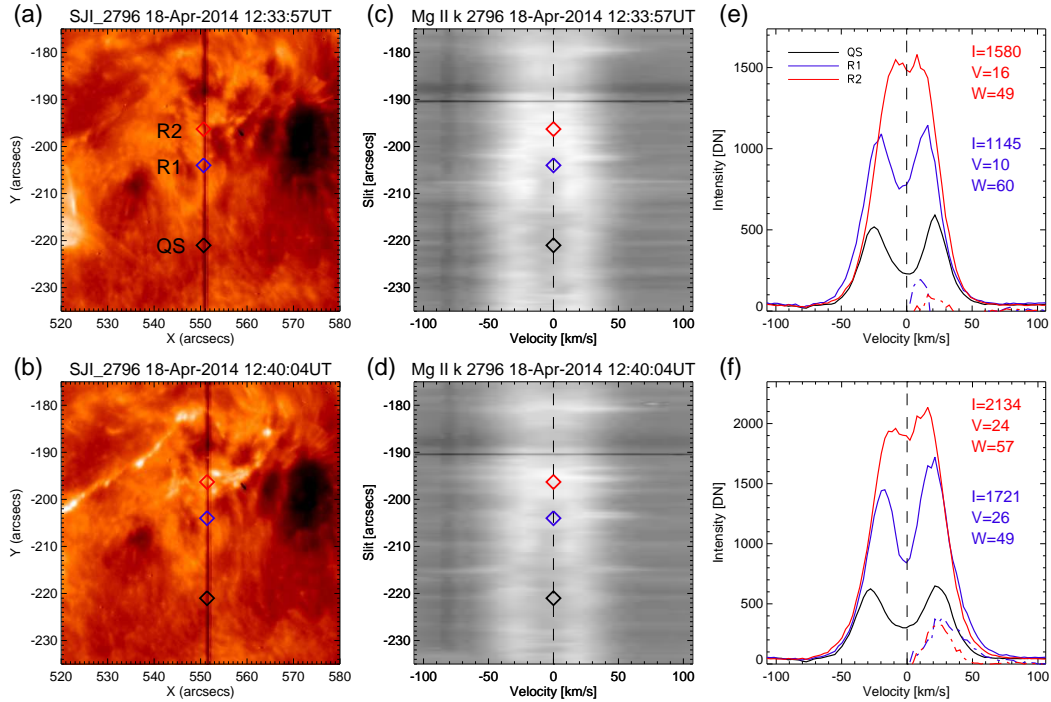


FIG. 7.— (a) and (b) *IRIS* 2796 Å SJI images displaying the footpoints of the MFR1 in the chromosphere. The red, blue, and black diamonds have the same meanings as in Figure 4. (c) and (d) Spectra of Mg II k 2796.347 Å at the slit. (e) and (f) Profiles of Mg II k 2796.347 Å at R1, R2, and QS. The dash-dotted curves denote the difference between the red wing and the blue wing.



a strong emission of the Si IV line. Moreover, such a strong emission is accompanied by a redshift of  $\geq 15$  km s $^{-1}$  and a non-thermal velocity of  $\sim 15$  km s $^{-1}$ . These features start from 13:33 UT, or probably earlier, lasting for  $\sim 13$  minutes, and then gradually become weaker as the flare impulsive phase commences. Note that, the large Doppler velocity and non-thermal velocity at some pixels in the flare ribbon may be problematic because the Si IV line there exhibits a second component at the red wing, thus invalidating the single Gaussian assumption.

The profiles of C II 1335.7077 Å generally deviate from a single Gaussian shape. At QS (Figure 6e and 6f), the profile is rather flat at the central part with its centroid slightly shifted to the red wing. Compared with the QS, the C II line at the footpoints of the MFR1 shows a stronger emission and is possibly double-peaked. At R2, the red peak is much stronger. But at R1, the profile shows a weak central absorption with still a slightly stronger red peak (Figure 6e). After the footpoints get strongly brightened, the emission is significantly enhanced especially at the red wing, which results in a more obvious line asymmetry. The intensities at the red peak increase by  $\sim 10$  times. Considering the significant line asymmetry and deviation from a single Gaussian, we adopt a simple method to derive the Doppler velocity. We subtract the intensity of the blue wing from the red one to get the residual emission whose peak is used to calculate the Doppler shift. Doing so is based on the assumption that the residual emission is from a moving plasma driven and heated by the reconnection in some place. In this way, the estimated Doppler velocities at R1 and R2 are  $\sim 30$  km s $^{-1}$  (Figure 6f).

Owing to its chromospheric origin, the profiles of Mg II k 2796.347 Å generally show a strong self-absorption in the line center due to a large opacity, in particular in the quiet region (e.g., at QS; Figure 7e and 7f). Leenaarts et al. (2013a,b) have studied in detail the diagnostic potential of this line at the quiet region based on radiation hydrodynamic simulations. Here, we present the characters of the line at the brightened region of the active region. At the footpoints of the MFR1, the line is enhanced with a reduced central absorption ( $k_3$ ) at R1 or even no central absorption at R2 (Figure 7e). If also applying the method of subtraction of the blue wing ( $k_{2v}$ ) from the red wing ( $k_{2r}$ ), the redshift velocity is estimated to be  $\sim 10$  and  $16$  km s $^{-1}$  at R1 and R2, respectively. With the brightness at the footpoints of the MFR1 increasing, the redshift velocity becomes somewhat larger, i.e.,  $\sim 26$  km s $^{-1}$  at R1 and  $\sim 24$  km s $^{-1}$  at R2 (Figure 7f).

#### 4.2.2. Blueshift at the Center of the MFR2

The Si IV 1402.77 Å line at the formation site of the MFR2 shows a very strong Doppler blueshift and a large FWHM when it brightens, as shown in Figure 8c. However, when the brightness drops and returns to the background, the blueshift and the excess broadening of the line almost disappear, as shown in Figure 8d. We also select three pixels at the slit, R1 and R2 in the center of the MFR2 (the intensity at R1 is larger than that at R2), and QS in the quiet region. The profiles of the Si IV line at the three pixels are shown in Figure 8e and 8f. One can clearly see that all the three profiles are singly peaked in spite of quite different peak intensities

(Figure 8f). The interesting fact is that when the line intensity increases, the line profile becomes broadened and asymmetric (Figure 8e). More specifically, the profile at R1 shows a stronger blue wing while that at R2 shows a stronger red wing. If we still use the single Gaussian fitting, the blueshift velocity is estimated to be  $\sim 34$  km s $^{-1}$  for R1 while the redshift velocity is  $\sim 18$  km s $^{-1}$  for R2.

The slit-time plots of the peak intensity, Doppler velocity, and non-thermal velocity at the slit of interest ( $y=[130'', 150'']$ ) are plotted in Figure 9. General speaking, the area with an enhanced brightness shows a strong Doppler blueshift velocity ( $\geq 20$  km s $^{-1}$ ) and non-thermal velocity ( $\geq 40$  km s $^{-1}$ ). Examining the profiles at R2, we find that they significantly deviate from a Gaussian shape especially at the blue wing. Considering the fact that the Mg II k line is blueshifted (Figure 11e and 11f), we suspect that the redshift at R2 could be due to an absorption at the blue wing. If this is the case, such an absorption could be caused by an upward moving plasma ejected from the chromosphere that is somewhat cooler and still absorptive relative to the background Si IV line emission. If adopting the method of the blue wing subtracted by the red one, the blueshift velocity is estimated to be  $\sim 39$  km s $^{-1}$  at R2 from an excess absorption and  $\sim 50$  km s $^{-1}$  at R1 from an excess emission. Note that not only the absolute values become significantly larger, but also the velocity sign is now different at R2, as compared with the results from the single Gaussian fitting.

Figure 10c and 10d present the spectra along the slit for C II 1335.7077 Å. The profile of this line shows an extremely strong self-absorption in the line center and a complicated shape at line wings when the central part of MFR2 brightens (Figure 10e). At R1, the blue wing is greatly enhanced, with emission even extending to  $-100$  km s $^{-1}$ . The blueshift velocity deduced from the blue wing subtracted by the red wing is  $\sim 46$  km s $^{-1}$ . While at R2, the blue wing is significantly reduced relative to that in the red wing, as in the case of the Si IV line. If we still ascribe it to an absorption, the absorbing plasma should have a velocity of  $\sim 52$  km s $^{-1}$ .

For the Mg II k 2796.347 Å line, when it gets brightened, it is highly broadened with a stronger central absorption, especially at R1 (Figure 11c and 11e). Meanwhile, the blue peak ( $k_{2v}$ ) is much stronger than the red peak ( $k_{2r}$ ). We notice that the absorption center ( $k_3$ ) does not change obviously. Therefore, we ascribe the stronger blue wing as being caused by a blueshifted emission. Using the difference profile between the blue wing and the red one, the blueshift velocity is estimated to be  $48$  km s $^{-1}$  at R1 and  $23$  km s $^{-1}$  at R2.

## 5. SUMMARY AND DISCUSSIONS

In this paper, we investigate the formation and initiation of two MFRs through imaging and spectral observations by AIA and *IRIS*. The EUV observations show that the magnetic field involved in the formation of the MFRs is primarily within in the core field of the active regions and is organized as two groups of sheared arcades. Their appearance only in the 131 Å and 94 Å passbands but not in other cooler passbands indicates that the arcades have a temperature of  $\geq 7$  MK. Through examining a sequence of line-of-sight magnetograms of the HMI (Figure 12 and attached movies), we find that the converging and shear-

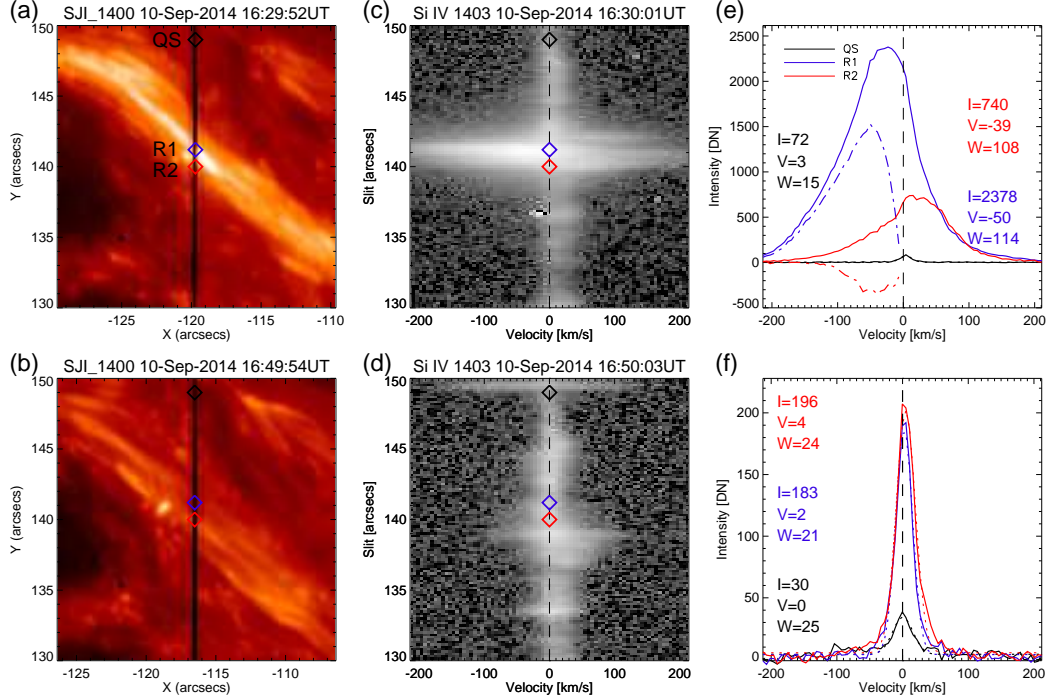


FIG. 8.— (a) and (b) *IRIS* 1400 Å SJI images displaying the center of the MFR2 in the transition region. The blue (R1) and red (R2) diamonds denote the two selected pixels at the MFR2 center, and the black one (QS) indicates one pixel at the quiet region. (c) and (d) Spectra of Si IV 1402.77 Å at the slit. (e) and (f) Profiles of Si IV 1402.77 Å at R1, R2, and QS. The profile of the blue wing subtracted by the corresponding red wing is shown as the dash-dotted curves.

(Animation of this figure is available in the online journal.)

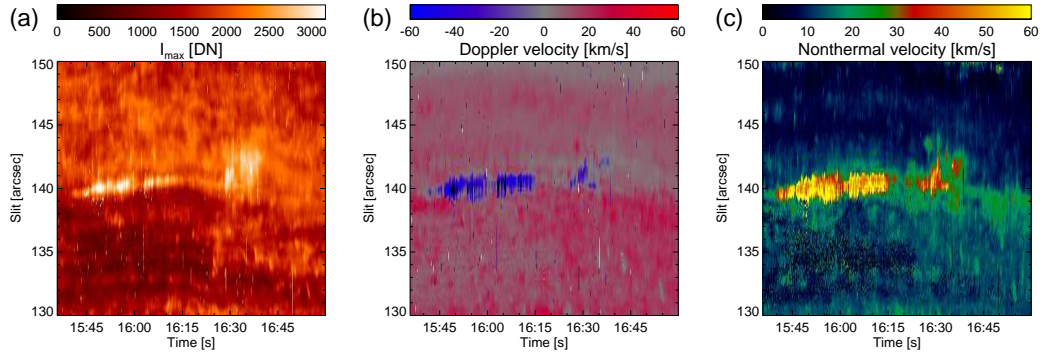


FIG. 9.— Slit-time plots of the peak intensity (a), Doppler velocity (b), and non-thermal velocity of the Si IV 1402.77 Å line at the slit for the 2014 September 10 event.

ing flows, as well as magnetic cancellation, occur near the main polarity inversion line. For the MFR1, some dispersive and weak opposite polarities move ceaselessly toward each other (Figure 12a–12c), resulting in magnetic cancellation near the possible formation site of the MFR1. For the MFR2, besides magnetic cancellation driven by the shearing flow, an obvious rotation of the preceding positive polarity also efficiently shears the arcades (Figure 12d–12f). Based on the observational properties, we suggest that the reconnection driven by the photospheric flows most likely take place and play a vital role in the formation of MFRs. On one hand, the reconnection may connect the head and end of two sheared arcades to form a continuous sigmoidal loop and accumulate the poloidal field of the MFR. On the other hand, it simultaneously heats the plasma in the MFR to make it only visible in the high temperature passbands of the AIA.

*IRIS* SJI images also provide valuable information to

understand the formation of the MFRs. Except for the brightening at the footpoints, other parts of the MFR1 are invisible in all the SJI images and AIA UV images, implying that its formation probably occurs mainly in the corona. While for the MFR2, it shows up not only in all AIA passbands but also in the *IRIS* 1400 Å and 2796 Å passbands, indicating that its formation likely takes place in the transition region and/or the chromosphere. Moreover, the finding of the cospatiality of the cool filamentary materials, which are visible in the AIA 304 Å and 171 Å passbands, with the brightened sigmoidal field also supports the hypothesis that the formation of the MFR2 may extend to the chromosphere.

The different formation altitudes between the MFR1 and MFR2 emphasizes the diversity of the reconnection locations, which can range from the photosphere to the corona. The results are consistent with the recent conclusions by Cheng et al. (2014b), in which they studied



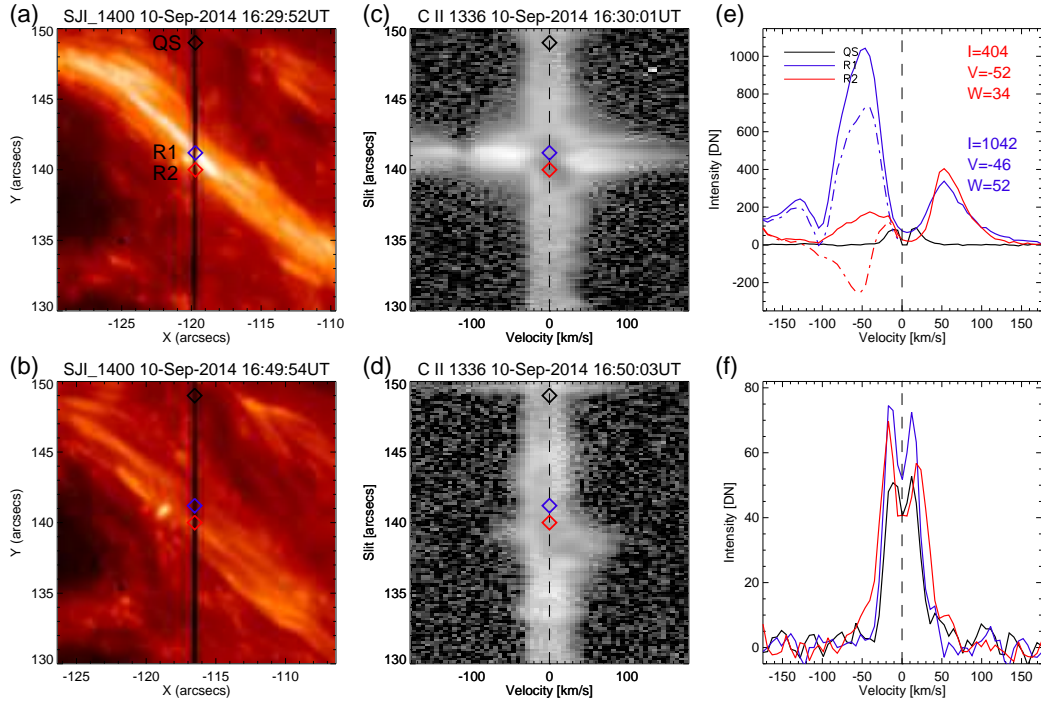


FIG. 10.— (a) and (b) *IRIS* 1400 Å SJI images displaying the center of the MFR2 in the transition region. The red, blue, and black diamonds have the same meanings as in Figure 8. (c) and (d) Spectra of C II 1335.7077 Å. (e) and (f) Profiles of C II 1335.7077 Å at R1, R2, and QS. The dash-dotted curves show the difference between the blue wing and the red wing.

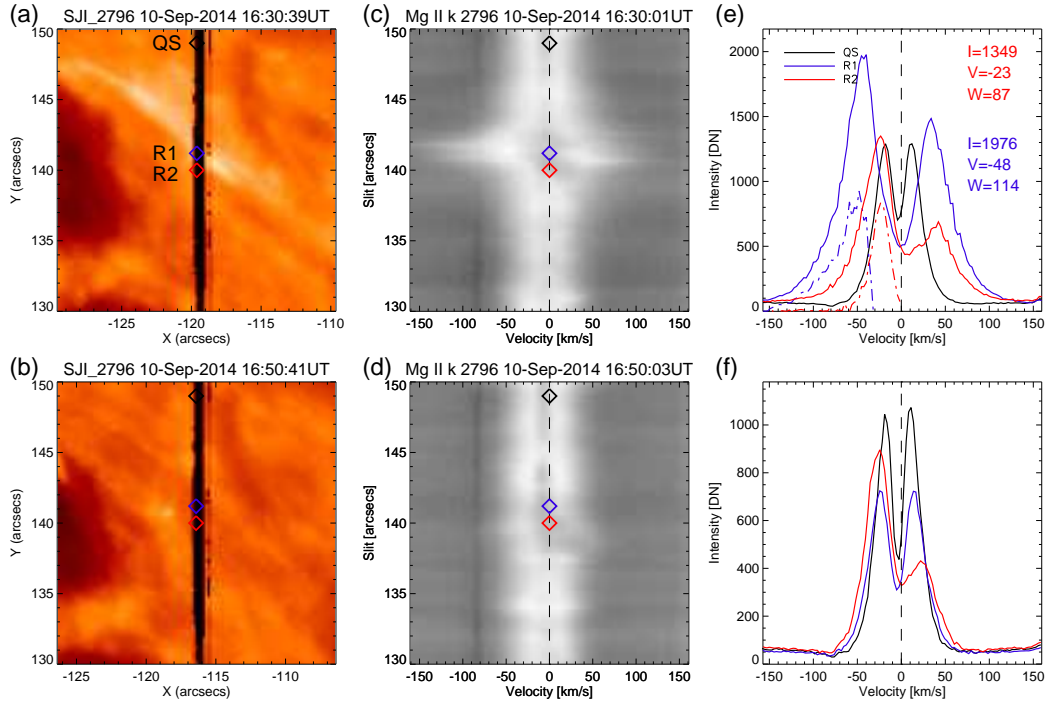


FIG. 11.— (a) and (b) *IRIS* 2796 Å SJI images displaying the MFR2 center in the chromosphere. The red, blue, and black diamonds have the same meanings as in Figure 8. (c) and (d) Spectra of Mg II k 2796.347 Å. (e) and (f) Profiles of Mg II k 2796.347 Å at R1, R2, and QS. The dash-dotted curves denote the profile of the blue wing subtracted by the red wing.

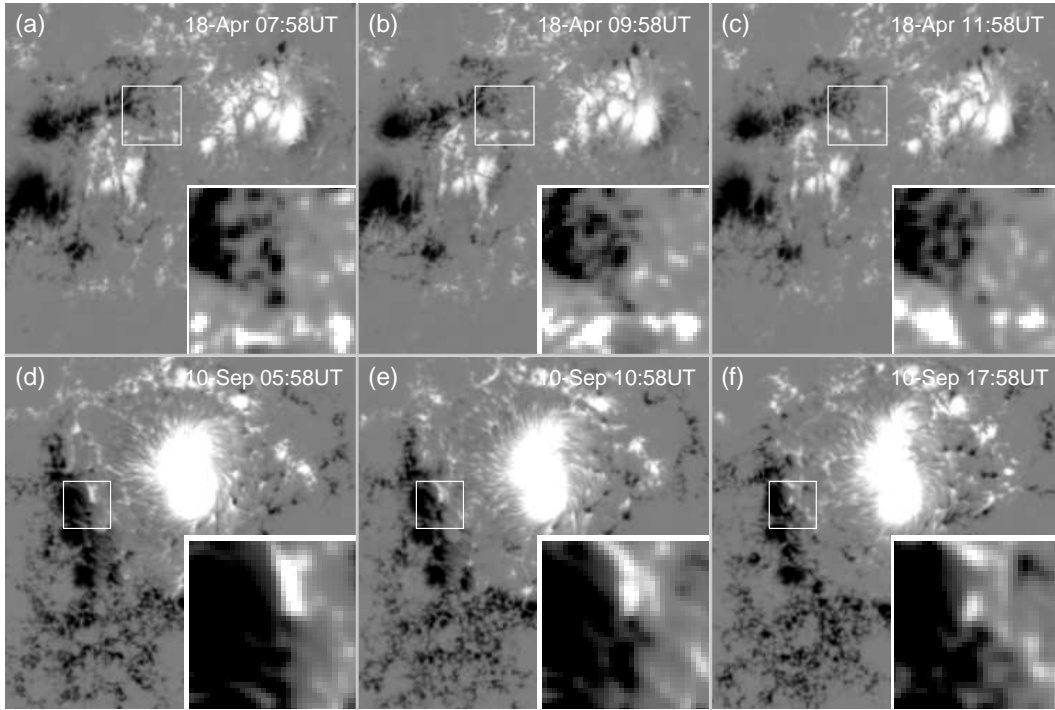


FIG. 12.— (a–c) A sequence of HMI line-of-sight magnetograms showing the convergence flow and magnetic cancellation near the formation site (white boxes) of the MFR1. (d–f) HMI line-of-sight magnetograms displaying the shearing flow and cancellation near the formation site (white boxes) of the MFR2.

(Animations of this figure are available in the online journal.)

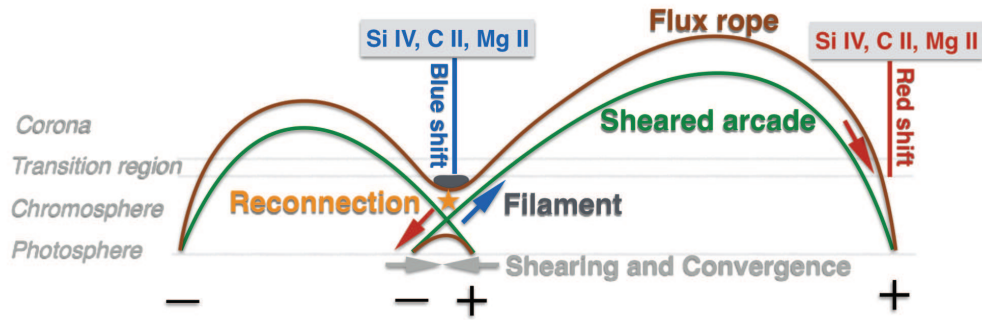


FIG. 13.— Schematic drawing of the formation of the MFR (brown) through the reconnection (yellow star) between two sheared arcades (green) in the chromosphere driven by the shearing and converging flows in the photosphere (grey arrows). The filament material (grey) is suspended in the magnetic dip of the MFR. The blueshift (blue arrow) and the redshift (red arrow) of the spectral lines (Si IV, C II, and Mg II) are observed at the center and footpoints of the MFR, respectively.

the long-term evolution of a sigmoidal active region and found that the twist in the core field gradually increases with reconnection continuously converting the sheared arcades to the sigmoidal field both at the bald-patch in the photosphere and in the hyperbolic flux tube in the corona.

*IRIS* spectral data further disclose some new features of the formation and initiation of the MFRs. For the MFR1, the Si IV, C II, and Mg II lines present a redshift and slightly large non-thermal velocity at the footpoints during the initiation phase. We interpret this as being caused by reconnect-induced outflow, which propagates along the legs of the MFR1 and finally reaches the lower atmosphere at the footpoints. Note that in flare ribbons, one can observe stronger redshift (or blueshift) and broadening of various lines that are mostly caused by chromospheric evaporation and/or condensation driven by the non-thermal electrons generated during the fast reconnection (Fisher et al. 1985; Li & Ding 2011; Tian et al. 2014a). In the case of the initiation of the MFR1, however, the redshift and broadening at the footpoints may instead be related to the outflow driven by the reconnection surrounding or inside the MFR1 that seems more gentle. Recent detection of a pre-flare enhancement of the non-thermal velocity at the footpoints of a CME (Harra et al. 2013) also supports such an interpretation.

For the MFR2, the *IRIS* slit is positioned at its formation site. Generally, the Si IV, C II, and Mg II lines show an extremely strong blueshift and non-thermal broadening at the most brightened pixels in the formation site. If it is still explained in terms of the reconnection scenario, then it requires that the reconnection has to occur in a place low enough so that either upward moving energetic electrons or reconnection outflow can heat the plasma above, and thus result in the blueshift and broadening of the Mg II, C II, and Si IV lines. Nevertheless, at some weakly brightened pixels at the formation site, the three lines display complicated patterns that seem puzzling. The Mg II line is blueshifted without ambiguity. However, the Si IV and C II lines exhibit a stronger red wing. Checking the line profiles, we are more inclined to the interpretation of an absorption at the blue wing, which can also be related to an upward moving plasma with a temperature not high enough to make it emissive relative to the Si IV and C II background emission (also see; Rouppe van der Voort et al. 2014). The reconnect-

tion scenario also expects the appearance of a downflow (e.g., Innes et al. 1997; Peter et al. 2014). However, for the MFR2, we only detect the upflow. A possible reason is that the downflow is kinetically less obvious than the upflow and could be smeared out in the spectra owing to the radiative transfer effect along the line of sight.

As a conclusion, based on the AIA and *IRIS* joint observations, we propose a cartoon for the formation of two MFRs, as shown in Figure 13. Two sheared arcades approach each other driven by the shearing and converging flows. The head of the left arcade and the end of the right arcade reconnects near the main polarity inversion line, forming a smaller loop and a longer MFR. Due to magnetic tension, the submergence of the small loop near the polarity inversion line, manifested as magnetic cancellation, is expected (Martin 1998). Meanwhile, the twisted MFR may rise up to the corona or still stay in the chromosphere depending on if there are filament materials suspended in the dips of the MFR. In the traditional tether-cutting model (Moore et al. 2001), the location of reconnection is not specified. Here, we suppose that the reconnection site is in the middle chromosphere, where the non-thermal particles accelerated during the reconnection can move upwards and lead to the large blueshift and strong broadening of the Si IV, C II, and even Mg II lines. The reconnection can also produces an obvious upward outflow, which can propagate along the field line of the MFR to the footpoint, thus making the Si IV, C II, and Mg II lines redshifted and weakly broadened.

We are grateful to the referee for his/her constructive comments that helped improve the manuscript. We also thank Hui Tian and Ying Li for the discussions on data calibration. *SDO* is a mission of NASAs Living With a Star Program. *IRIS* is a NASA small explorer mission developed and operated by LMSAL with mission operations executed at NASA Ames Research center and major contributions to downlink communications funded by the Norwegian Space Center (NSC, Norway) through an ESA PRODEX contract. X.C., M.D.D., and F.C. are supported by NSFC under grants 11303016, 11373023, and NKBRSF under grants 2011CB811402 and 2014CB744203. X.C. is also supported by Key Laboratory of Solar Activity of National Astronomical Observatories of the Chinese Academy of Sciences by Grant KLSA201311.

## REFERENCES

- Amari, T., Aly, J.-J., Luciani, J.-F., Mikic, Z., & Linker, J. 2011, *ApJ*, 742, L27
- Amari, T., Canou, A., & Aly, J.-J. 2014, *Nature*, 514, 465
- Antiochos, S. K., DeVore, C. R., & Klimchuk, J. A. 1999, *ApJ*, 510, 485
- Archontis, V., & Török, T. 2008, *A&A*, 492, L35
- Aulanier, G., Török, T., Démoulin, P., & DeLuca, E. E. 2010, *ApJ*, 708, 314
- Bak-Stęślicka, U., Gibson, S. E., Fan, Y., Bethge, C., Forland, B., & Rachmeler, L. A. 2013, *ApJ*, 770, L28
- Burlaga, L., Sittler, E., Mariani, F., & Schwenn, R. 1981, *J. Geophys. Res.*, 86, 6673
- Canfield, R. C., Hudson, H. S., & McKenzie, D. E. 1999, *Geophys. Res. Lett.*, 26, 627
- Chen, B., Bastian, T. S., & Gary, D. E. 2014a, *ApJ*, 794, 149
- Chen, H., Zhang, J., Cheng, X., Ma, S., Yang, S., & Li, T. 2014b, *ArXiv e-prints*
- Chen, P. F. 2011, *Living Reviews in Solar Physics*, 8, 1
- Cheng, X., Ding, M. D., Zhang, J., Srivastava, A. K., Guo, Y., Chen, P. F., & Sun, J. Q. 2014a, *ApJ*, 789, L35
- Cheng, X., Ding, M. D., Zhang, J., Sun, X. D., Guo, Y., Wang, Y. M., Kliem, B., & Deng, Y. Y. 2014b, *ApJ*, 789, 93
- Cheng, X., Zhang, J., Ding, M. D., Liu, Y., & Poomvises, W. 2013a, *ApJ*, 763, 43
- Cheng, X., Zhang, J., Ding, M. D., Olmedo, O., Sun, X. D., Guo, Y., & Liu, Y. 2013b, *ApJ*, 769, L25
- Cheng, X., Zhang, J., Liu, Y., & Ding, M. D. 2011, *ApJ*, 732, L25
- Cheng, X., et al. 2014c, *ApJ*, 780, 28
- De Pontieu, B., et al. 2014, *Sol. Phys.*, 289, 2733
- Dove, J. B., Gibson, S. E., Rachmeler, L. A., Tomczyk, S., & Judge, P. 2011, *ApJ*, 731, L1
- Fan, Y. 2001, *ApJ*, 554, L111
- Fan, Y., & Gibson, S. E. 2004, *ApJ*, 609, 1123
- Fisher, G. H., Canfield, R. C., & McClymont, A. N. 1985, *ApJ*, 289, 425



- Gibson, S. E., & Fan, Y. 2006, *Journal of Geophysical Research (Space Physics)*, 111, 12103
- Gibson, S. E., Foster, D., Burkepile, J., de Toma, G., & Stanger, A. 2006, *ApJ*, 641, 590
- Green, L. M., & Kliem, B. 2009, *ApJ*, 700, L83
- Green, L. M., Kliem, B., & Wallace, A. J. 2011, *A&A*, 526, A2
- Guo, Y., Schmieder, B., Démoulin, P., Wiegmann, T., Aulanier, G., Török, T., & Bommier, V. 2010, *ApJ*, 714, 343
- Harra, L. K., Matthews, S., Culhane, J. L., Cheung, M. C. M., Kontar, E. P., & Hara, H. 2013, *ApJ*, 774, 122
- Innes, D. E., Inhester, B., Axford, W. I., & Wilhelm, K. 1997, *Nature*, 386, 811
- Inoue, S., Hayashi, K., Shiota, D., Magara, T., & Choe, G. S. 2013, *ApJ*, 770, 79
- Jiang, C., Wu, S. T., Feng, X., & Hu, Q. 2014, *ApJ*, 780, 55
- Karpen, J. T., Antiochos, S. K., & DeVore, C. R. 2012, *ApJ*, 760, 81
- Kliem, B., Titov, V. S., & Török, T. 2004, *A&A*, 413, L23
- Kumar, P., & Cho, K.-S. 2014, *A&A*, 572, A83
- Kumar, P., Srivastava, A. K., Filippov, B., Erdélyi, R., & Uddin, W. 2011, *Sol. Phys.*, 272, 301
- Leake, J. E., Linton, M. G., & Török, T. 2013, *ApJ*, 778, 99
- Leenaarts, J., Pereira, T. M. D., Carlsson, M., Uitenbroek, H., & De Pontieu, B. 2013a, *ApJ*, 772, 89
- . 2013b, *ApJ*, 772, 90
- Lemen, J. R., et al. 2012, *Sol. Phys.*, 275, 17
- Li, L. P., & Zhang, J. 2013a, *A&A*, 552, L11
- Li, T., & Zhang, J. 2013b, *ApJ*, 770, L25
- Li, X., Morgan, H., Leonard, D., & Jeska, L. 2012, *ApJ*, 752, L22
- Li, Y., & Ding, M. D. 2011, *ApJ*, 727, 98
- Liu, R., Liu, C., Wang, S., Deng, N., & Wang, H. 2010, *ApJ*, 725, L84
- Liu, R., Wang, Y., & Shen, C. 2014a, *ApJ*, 797, 37
- Liu, Y. D., et al. 2014b, *Nature Communications*, 5, 3481
- Low, B. C., & Hundhausen, J. R. 1995, *ApJ*, 443, 818
- Lynch, B. J., Antiochos, S. K., DeVore, C. R., Luhmann, J. G., & Zurbuchen, T. H. 2008, *ApJ*, 683, 1192
- Mackay, D. H., Karpen, J. T., Ballester, J. L., Schmieder, B., & Aulanier, G. 2010, *Space Sci. Rev.*, 151, 333
- Manchester, IV, W., Gombosi, T., DeZeeuw, D., & Fan, Y. 2004, *ApJ*, 610, 588
- Martin, S. F. 1998, *Sol. Phys.*, 182, 107
- Moore, R. L., Sterling, A. C., Hudson, H. S., & Lemen, J. R. 2001, *ApJ*, 552, 833
- Patsourakos, S., Vourlidas, A., & Stenborg, G. 2013, *ApJ*, 764, 125
- Pesnell, W. D., Thompson, B. J., & Chamberlin, P. C. 2012, *Sol. Phys.*, 275, 3
- Peter, H., et al. 2014, *Science*, 346, C315
- Régnier, S., Walsh, R. W., & Alexander, C. E. 2011, *A&A*, 533, L1
- Roupe van der Voort, L., De Pontieu, B., Pereira, T. M. D., Carlsson, M., & Hansteen, V. 2014, *ArXiv e-prints*
- Savcheva, A. S., van Ballegoijen, A. A., & DeLuca, E. E. 2012, *ApJ*, 744, 78
- Schou, J., et al. 2012, *Sol. Phys.*, 275, 229
- Song, H. Q., Zhang, J., Chen, Y., & Cheng, X. 2014, *ApJ*, 792, L40
- Sterling, A. C., Hudson, H. S., Thompson, B. J., & Zarro, D. M. 2000, *ApJ*, 532, 628
- Su, Y., & van Ballegoijen, A. 2012, *ApJ*, 757, 168
- Tian, H., Li, G., Reeves, K. K., Raymond, J. C., Guo, F., Liu, W., Chen, B., & Murphy, N. A. 2014a, *ApJ*, 797, L14
- Tian, H., Young, P. R., Jaeggli, S., Curdt, W., Daw, A., Pereira, T. M., De Pontieu, B., & Reeves, K. K. 2015, *ApJ submitted*
- Tian, H., et al. 2014b, *ApJ*, 786, 137
- Wang, J., & Shi, Z. 1993, *Sol. Phys.*, 143, 119
- Wang, Y.-M., & Stenborg, G. 2010, *ApJ*, 719, L181
- Xia, C., Keppens, R., & Guo, Y. 2014, *ApJ*, 780, 130
- Yang, S., Zhang, J., Liu, Z., & Xiang, Y. 2014, *ApJ*, 784, L36
- Zhang, J., Cheng, X., & Ding, M.-D. 2012, *Nature Communications*, 3, 747
- Zhang, J., et al. 2007, *Journal of Geophysical Research (Space Physics)*, 112, 10102